Magnetic fields on FIRE: Comparing B-fields in the multiphase ISM and CGM of simulated L$_*$ galaxies to observations

Sam B. Ponnada [ID],[1]★ Georgia V. Panopoulou [ID],[1]† Iryna S. Butsky [ID],[1] Philip F. Hopkins [ID],[1] Sarah R. Loebman,[2] Cameron Hummels,[1] Suoqing Ji,[3] Andrew Wetzel [ID],[4] Claude-André Faucher-Giguère[5] and Christopher C. Hayward [ID][6]

[1]*California Institute of Technology, TAPIR, Mailcode 350-17, Pasadena, CA 91125, USA*
[2]*Department of Physics, University of California, Merced, 5200 N. Lake Road, Merced, CA 95343, USA*
[3]*Astrophysics Division and Key Laboratory for Research in Galaxies and Cosmology, Shanghai Astronomical Observatory, Chinese Academy of Sciences, Shanghai 200030, China*
[4]*Department of Physics and Astronomy, University of California, Davis, CA 95616, USA*
[5]*Department of Physics and Astronomy and CIERA, Northwestern University, 2145 Sheridan Road, Evanston, IL 60208, USA*
[6]*Center for Computational Astrophysics, Flatiron Institute, 162 Fifth Avenue, New York, NY 10010, USA*

ABSTRACT

The physics of magnetic fields (**B**) and cosmic rays (CRs) have recently been included in simulations of galaxy formation. However, significant uncertainties remain in how these components affect galaxy evolution. To understand their common observational tracers, we analyse the magnetic fields in a set of high-resolution, magnetohydrodynamic, cosmological simulations of Milky-Way-like galaxies from the FIRE-2 project. We compare mock observables of magnetic field tracers for simulations with and without CRs to observations of Zeeman splitting and rotation/dispersion measures. We find reasonable agreement between simulations and observations in both the neutral and the ionized interstellar medium (ISM). We find that the simulated galaxies with CRs show weaker ISM |**B**| fields on average compared to their magnetic-field-only counterparts. This is a manifestation of the effects of CRs in the diffuse, low density inner circumgalactic medium (CGM). We find that equipartition between magnetic and cosmic ray energy densities may be valid at large ($>$ 1 kpc) scales for typical ISM densities of Milky-Way-like galaxies, but not in their haloes. Within the ISM, the magnetic fields in our simulated galaxies follow a power-law scaling with gas density. The scaling extends down to neutral hydrogen number densities $<$ 300 cm^{-3}, in contrast to observationally derived models, but consistent with the observational measurements. Finally, we generate synthetic rotation measure (RM) profiles for projections of the simulated galaxies and compare to observational constraints in the CGM. While consistent with upper limits, improved data are needed to detect the predicted CGM RMs at 10–200 kpc and better constrain theoretical predictions.

Key words: cosmic rays – ISM: magnetic fields – galaxies: formation – galaxies: haloes – galaxies: magnetic fields.

1 INTRODUCTION

Magnetic fields are of considerable importance in galaxies, as they are a substantial source of pressure support in the interstellar medium (ISM) and circumgalactic medium (CGM) (Beck 2015). They are capable of significantly influencing the dynamics of both fully ionized gas and star-forming molecular clouds, thereby modulating star formation rates (for a review, see Krumholz & Federrath 2019). Magnetic fields also determine the propagation of cosmic rays (CRs) throughout the ISM and into the CGM (Fermi 1949; Kulsrud & Pearce 1969; Desiati & Zweibel 2014; Shukurov et al. 2017). Despite their well-established physical significance, magnetic fields and their connection to galaxy evolution have yet to be fully understood, with progress limited by the ability to accurately characterize magnetic

field strengths and topologies. Obtaining accurate measurements of the magnetic field strength and geometry in and around galaxies has implications for many open questions, including their origins and amplification, as well their role in providing non-thermal pressure support and influencing the physical state of the ISM and CGM (Butsky et al. 2017; Hopkins et al. 2018; Ji, Oh & McCourt 2018; Rodrigues et al. 2019; Ntormousi et al. 2020; Pakmor et al. 2020).

Obtaining reliable observational measurements of the field strengths and topologies remains difficult. Most observable tracers of the magnetic field are indirect and rely on certain assumptions: most notably, that of equipartition between CR and magnetic energy densities. Assuming equipartition/minimum-energy was first employed to determine field strengths in the jet of M87 by Burbidge (1956), and has been utilized to determine galactic field strengths (Beck 2000; Chyzy et al. 2011; Fletcher et al. 2011; Beck 2015). These estimates utilize the total synchrotron intensity to give information about the magnetic field in the plane of the sky, perpendicular to our line of sight ($B_\perp$), which is used to infer the total magnetic field

★ E-mail: sponnada@caltech.edu
† Hubble Fellow.

strength (B_{tot}). As Beck (2015) delineates, this method of estimating magnetic field strengths is not without caveats; variation of B along the line of sight (LOS) or within the telescope beam (Beck et al. 2003), energy losses of CR electrons (Beck & Krause 2005), and invalidity of equipartition on small scales can all lead to overestimating or underestimating the true field strength (Stepanov et al. 2014).

Other observational measurements of magnetic field strengths are sensitive to the field component parallel to the LOS ($B_{\parallel}$) convolved with various LOS plasma properties, and uncertain ISM phase structure. These include measurements from Zeeman splitting of spectral lines, which probes the cold, atomic ISM (e.g. Crutcher et al. 2010; Crutcher 2012) as well as the use of the ratio of the rotation measure (RM) and dispersion measure (DM) towards background sources like pulsars or fast radio bursts (FRBs) (Han, Manchester & Qiao 1999; Lan & Prochaska 2020; Seta & Federrath 2021), which probe the highly ionized phases. Both Zeeman splitting and RM/DM are sensitive to the direction of the magnetic field along the LOS, and measure the magnitude of the regular (ordered and coherent) field component, weighted differently by properties like gas density. It is worth noting that inferring magnetic field strengths from RM/DM relies on the assumption that the thermal electron density and magnetic field strength are uncorrelated (Beck 2015; Seta & Federrath 2021).

A common thread amongst measurements of magnetic fields in galaxies is reliance on several simplifying assumptions which may or may not hold in the multiphase ISM and CGM. This provides motivation for exploring the validity of these assumptions from a theoretical perspective, along with the relative paucity of forward modelled predictions for RM/DM and Zeeman inferred measurements of magnetic fields, especially in cosmological simulations of galaxy formation with amplification from primordial fields. Furthermore, CRs have only recently been included in simulations of galaxy formation, allowing for physics prescriptions which can notably change properties of the ISM and CGM, as well as the potential to forward model synchrotron emissivities (Pakmor et al. 2016; Hopkins et al. 2020; Pfrommer et al. 2021; Werhahn, Pfrommer & Girichidis 2021).

It is only recently that simulations of galaxy formation that included magnetic fields have been capable of following the evolution of galaxies over cosmic time while resolving the ISM (for example, Marinacci, Pakmor & Springel 2014; Pakmor, Marinacci & Springel 2014; Rieder & Teyssier 2017; Hopkins et al. 2018). Previously, galaxy-scale simulations that included magnetic field information were often limited to mostly idealized, non-cosmological simulations (Wang & Abel 2009; Pakmor & Springel 2013; Butsky et al. 2017; Su et al. 2017; Steinwandel et al. 2019, 2020, 2022). Within state-of-the-art simulations, models for feedback and their numerical implementations vary considerably. It has been shown that including essential physics such as gas cooling, star formation, and feedback from stars results in different magnetic field saturation strengths and morphologies (Rieder & Teyssier 2017; Su et al. 2018).

Previous work which analysed magnetic fields includes Hopkins et al. (2020), who used a set of simulations with magnetic fields and magnetic fields including CRs (which are also analysed in this study) to demonstrate that magnetic pressure appears to be generally subdominant to thermal pressure ($\beta = P_{thermal}/P_{magnetic} >> 1$), especially in the CGM, though this study did not closely analyse the magnetic field strengths in the dense ISM, where conditions can be markedly different. They also found that field morphology is tangled on all scales, and found hints of observationally relevant trends with regards to clumping factors, equipartition, and halo gas

distributions, but they did not perform a detailed comparison of the magnetic fields with observations.

Cosmic rays have been found to have little impact on the magnetic field structure and strength in the CGM, however, they have been shown to significantly influence on the dynamics and phase structure of gas in the disc–halo interface, which is the region within 10 kpc vertically from the disc plane (Ji et al. 2020; Chan et al. 2021). The resulting impact on the recycling of outflows, i.e. fountain flows, may be of considerable importance to the amplification of magnetic fields (Anglés-Alcázar et al. 2017; Su et al. 2017; Martin-Alvarez et al. 2018). But again, these analyses were not focused on observational comparison.

Despite efforts in understanding the physical implications of magnetic fields and CRs on galactic properties, specifically in the CGM, there have been few forward-modelled observations from idealized and cosmological simulations with explicit treatment of magnetic fields and/or CRs (e.g. Pakmor et al. 2018; Pfrommer et al. 2021; van de Voort et al. 2021; Werhahn et al. 2021), and little focus on magnetic fields in the ISM of simulated galaxies (though, see Guszejnov et al. 2020; Pakmor et al. 2020; Rappaz, Schober & Girichidis 2022).

In this study, we present analyses of six cosmological 'zoom-in' simulations from the Feedback in Realistic Environments Project (FIRE-2[1]), described in Section 2. We aim to compare synthetic observational tracers of magnetic fields to observed quantities in both the ISM and CGM of L_* galaxies. This is done for two different physical models, one including cosmic rays and one without, and we discuss how the inclusion of CRs impacts the magnetic fields and their observational tracers in Section 3. We also investigate the degree to which the simulated galaxies' magnetic fields and tracers match observations. In Section 4, we compare our results in context of other relevant work, and in Section 5, we summarize our results and discuss future work on probing galactic magnetic fields through synthetic observations.

2 SIMULATIONS AND METHODS

We refer the reader to Hopkins et al. (2020) and references therein for extensive details on the simulations. Here we summarize the most relevant information, and list the fundamental properties of each simulation in Table 1. The simulations analysed here are part of the second iteration of the FIRE project, FIRE-2 (see Hopkins et al. 2018), and so include the physics of gas cooling, explicit treatment of stellar feedback (stellar winds, radiation, and SNe), with the set analysed in this study including magnetic fields, cosmic rays, and fully anisotropic conduction and viscosity. These simulations are fully cosmological, with adaptive treatment of hydrodynamics and gravity in gas cells, and constant softening parameters for stellar and dark matter particles. The equations of ideal magnetohydrodynamics (MHD) are solved, and simulations with cosmic rays include an ultrarelativistic fluid ($\gamma = 4/3$) treatment of CRs with injection from SNe and fully anisotropic streaming, advective and diffusive terms, loss terms, and gas coupling. The injection of CRs from SNe is done by assuming 10 per cent of the fiducial SNe energy of 10^{51} erg goes to CRs and is coupled to gas adjacent to the SNe site. Since it is thought that CRs with energies of ~ 1 GeV dominate the CR energy density in L_* galaxies, the CR energy density is evolved for CR energies only around this value (Boulares & Cox 1990). In this study, the simulations with cosmic rays assume a constant effective diffusion

[1] https://fire.northwestern.edu/

Table 1. Simulation properties for the simulations analysed in this study, from Hopkins et al. (2020). The columns show the halo's virial mass at $z = 0$ following (Bryan & Norman 1998), the galaxy's stellar mass in the MHD+ and CR+ simulations at $z = 0$, the galaxy's average magnetic field strength in the disc at $z = 0$ (defined as the mass-averaged magnetic field strength in all gas cells in the disc), the mass-averaged magnetic field strength in all gas cells in the inner CGM (50 kpc $< r <$ 100 kpc), the mass-averaged magnetic field strength in all gas cells in the outer CGM (100 kpc $< r <$ 240 kpc), and a short description of each galaxy. We show only the CR+ $< |\mathbf{B}| >_{\mathrm{CGM}}^{\mathrm{CR}}$ as at large radii from the galaxy, $<|\mathbf{B}| >$ is nearly identical between MHD+ and CR+ simulations (Fig. 9).

Simulation	$M_{\mathrm{halo}}^{\mathrm{vir}}$ ($\mathrm{M_\odot}$)	M_*^{MHD} ($\mathrm{M_\odot}$)	M_*^{CR} ($\mathrm{M_\odot}$)	$< |\mathbf{B}| >_{\mathrm{disc}}^{\mathrm{MHD}}$ (μG)	$< |\mathbf{B}| >_{\mathrm{disc}}^{\mathrm{CR}}$ (μG)	$< |\mathbf{B}| >_{\mathrm{inner\,CGM}}^{\mathrm{CR}}$ (μG)	$< |\mathbf{B}| >_{\mathrm{outer\,CGM}}^{\mathrm{CR}}$ (μG)	Description
m12i	1.2e12	7e10	3e10	7.93	3.99	0.025	0.012	Late forming MW-mass halo with a massive disc
m12f	1.6e12	8e10	4e10	5.36	4.64	0.024	0.011	MW-like disc with a LMC-like satellite merger
m12m	1.5e12	1e11	3e10	10.65	1.78	0.012	0.008	Earlier forming halo with strong bar at lower redshift

coefficient $\kappa = $ 3e29 cm^2 s^{-1}, which is observationally motivated (Chan et al. 2019).

We focus only on the most massive galaxy in each of three zoom-in volumes, galaxies roughly akin in mass and size to the Milky-Way, which are named m12i, m12f, and m12m (see Table 1). Note that while the runs analysed in this study are not publicly available, snapshots of the FIRE-2 simulations with the fiducial treatment of feedback physics are publicly available[2] (Wetzel et al. 2022). Some important systematic trends are notable between the simulations modelling MHD and those modelling MHD including cosmic rays (hereafter denoted MHD+ and CR+, respectively). One of these systematic trends is that the CR+ galaxies are $\sim$ 2–3 times lower in stellar mass than their MHD+ counterparts. The reason for the systematically lower stellar masses in the CR+ galaxies is explained in Hopkins et al. (2020), Ji et al. (2020, 2021) as CR pressure support in the CGM preventing gas for star formation from precipitating on to the disc at redshift $z \lesssim$ 1–2. Correspondingly, the CR+ simulations also tend to have systematically lower ISM gas masses, gas densities, and star-formation rates (SFRs), as well as lower ($\sim$ 20 per cent) neutral hydrogen velocity dispersions in the inner disc, $\pm$ 250 pc vertically from the disc mid-plane (Chan et al. 2021).

When we calculate line-of-sight integrated quantities, we project the galaxy face-on or edge-on using the angular momentum vector of the stars to define the direction perpendicular to the galactic disc, which we use as the z component. Every particle position and vector field in the simulation is transformed accordingly, and this is the coordinate frame in which we define spatial regions below. We integrate gas quantities using the method of Hopkins et al. (2005) along a set of lines of sight (LOSs) which uniformly sample the desired area. The sampling is done by dividing the area of interest into a 2D, 700 $\times$ 700 image, with little to no difference in the results when increasing the image resolution. The required magnetic fields and gas quantities such as temperature and ionization state are calculated self-consistently in-code (Hopkins 2015; Hopkins et al. 2018, 2020).

For ISM quantities, we restrict LOS integrations to gas within a cylindrical region of 14 kpc to account for the extent of our galaxies' gas discs (Bellardini et al. 2021) and height $|z| <$ 1 kpc, though none of our results are especially sensitive to the exact threshold. If we restrict to 'Solar Circle' radii, we only include cells with galactocentric radii, R, that satisfy: 7 kpc $< R <$ 9 kpc. Furthermore, since the Milky-Way pulsar observations we compare to (3.4) sample typical distances to sources between $\sim$0.1–4 kpc, we divide the ISM integration into 'slabs' uniformly sampling varying

depths in log(distance) over this range; we agglomerate a collection of sightlines through the disc with slabs of thickness in z of 0.1, 0.2, 0.5, 1, 2, and 4 kpc. This is equivalent to placing sources and observers randomly in order to sample a similar distance distribution to the observations. For CGM quantities, we integrate sightlines through a sphere of physical radius $r = $ 245 kpc, corresponding to a projected radius of 200 kpc centred on the galaxy. We define the physical radius to be $r = \sqrt{x^2 + y^2 + z^2}$, while the projected galactocentric radius is $R = \sqrt{x^2 + y^2}$ for a face-on projection and $R = \sqrt{x^2 + z^2}$ for an edge-on projection (where x, y, z are all centred on the galaxy centre).

3 RESULTS

3.1 Magnetic fields versus gas density in the ISM

We first investigate the relation between the magnetic field, $\mathbf{B}$, and gas density, n_{H}, in the simulations, within the ISM. Throughout this work, we often refer to the magnetic field in the simulation as the 'true' magnetic field to distinguish from observationally derived magnetic field measures. We select all gas cells in the discs, i.e. cells with z coordinate $|z| <$ 1 kpc and galactocentric radius $R = \sqrt{x^2 + y^2} <$ 14 kpc, where x, y refer to the coordinates of the cell in the simulation volume.

The relation of $|\mathbf{B}|$ with n_{H} for the different MHD+ and CR+ simulations is shown in Fig. 1. In our simulations, $|\mathbf{B}| \sim n_{\mathrm{H}}^\alpha$ for typical ISM gas densities ($n_{\mathrm{H}} \gtrsim 1$ cm^{-3}), where α is a power-law fit to the mean and ranges around $\sim$ 0.5–0.6. In a simplistic case where the exponent α is set by the collapse of gas in the absence of magnetic flux diffusion (flux freezing), α is related to the geometry of the collapse. The value of α can range from 0, if gas collapses along magnetic field lines, to 1, if the collapse is perpendicular to field lines, while the case of isotropic collapse gives an exponent of $\alpha = 2/3$ (Crutcher et al. 2010; Crutcher 2012; Tritsis et al. 2015). Our simulations exhibit a scatter in the slope of the relation consistent with the resulting trend from isotropic flux freezing, $|\mathbf{B}| \sim n_{\mathrm{H}}^{2/3}$ (or $|\mathbf{B}| \sim n_{\mathrm{H}}^{1/2}$ in the case where the assumption of spherical cloud geometry is invalid). $|\mathbf{B}| \sim n_{\mathrm{H}}^{1/2}$ is preferred where the cloud geometry is more slab-like or filamentary, with field lines perpendicular to the slab, or at an angle relative to the primary axis of the filament, which collapses radially (see Tritsis et al. 2015, for a detailed discussion).

At lower densities, $n_{\mathrm{H}} \ll 1$ cm^{-3}, we find different behaviours for the MHD+ and CR+ simulations. While the mean values of $|\mathbf{B}|$ in the MHD+ and CR+ relations mostly agree at typical ISM densities (the mean ISM number density for these simulated galaxies is $\sim$ a few cm^{-3}, with a standard deviation of ~ 100 cm^{-3}), there is a substantial
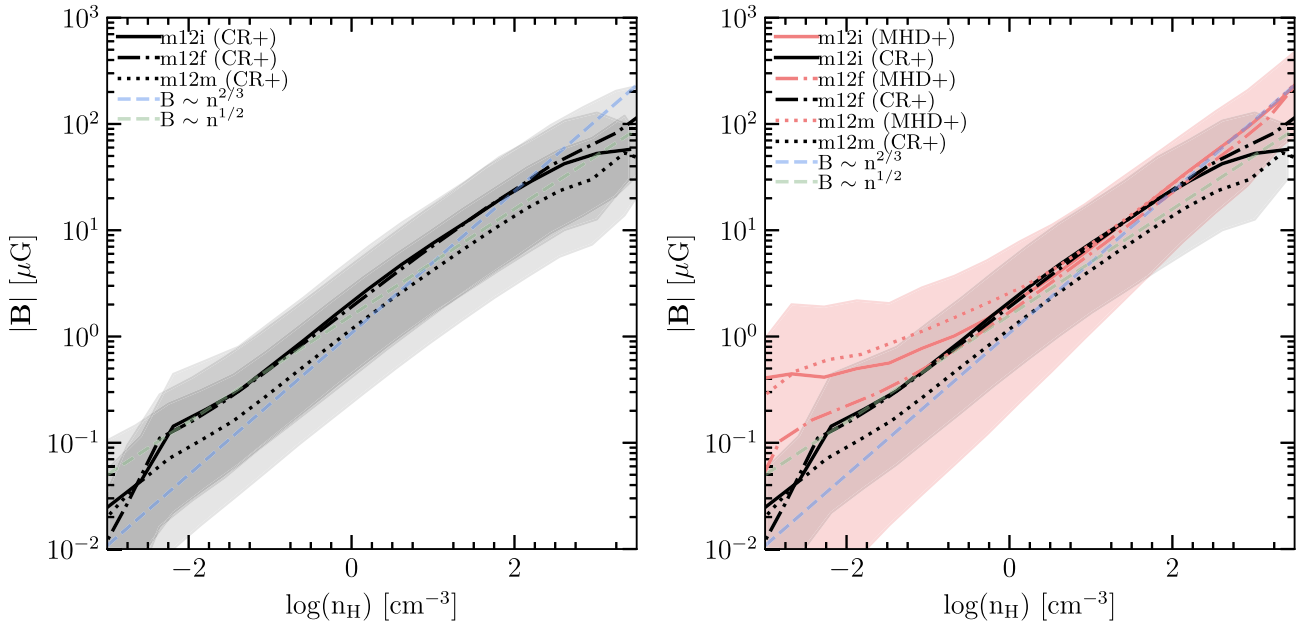
Figure 1. Mean |**B**| versus gas number density, n_H, for all gas cells in the galactic disc. Left-hand panel: Mean |**B**| at each n_H bin for each of the three CR+ simulations (black lines as described in legend). The shaded regions represent the 5–95 percentile range. Scaling relations expected for isotropic flux freezing, with and without spherical geometry of |**B**| $\sim n_H^{2/3}$ and $n_H^{1/2}$ are also shown (blue and green dashed lines, respectively). Right-hand panel: Mean |**B**| at each n_H bin for m12i (MHD+) in coral, and the same for the CR+ run in black. Owing to second-order dynamical effects in the 'inner CGM,' CR+ simulations exhibit suppressed magnetic field strengths at low gas densities ($n_H < 0.1$ cm^{-3}). All of our simulations show roughly the same power-law scaling relation in |**B**| versus n_H, consistent with that of isotropic flux-freezing, with subtle normalization differences due to galaxy–galaxy variation.

offset (of a factor of 2–10) in the very diffuse gas, at number densities less than 0.01 cm^{-3}. For m12i and m12m, shown in the right-hand panel of Fig. 1, the CR+ simulations exhibit suppressed mean |**B**| values compared to the MHD+ simulations. For m12f, however, there is no significant offset. When comparing among the CR+ runs, we find only modest galaxy-to-galaxy differences in their |**B**| – n_H relations. While m12i (CR+) and m12f (CR+) exhibit very similar trends in |**B**| versus n_H, we find that m12m (CR+) has a mean |**B**| systematically lower at a given gas density at $n_H > 1$ cm^{-3} by a factor[3] of ~ 2. The origin of these galaxy-to-galaxy variations may arise in the specific merger histories of the galaxies, as m12m has a considerably different merger history than m12i and m12f, with m12m (CR+) also exhibiting the largest difference in stellar mass from its MHD+ counterpart, or due to its different gas and stellar mass profiles and morphology (see Hopkins et al. 2020), but we are unable to identify any single variable that explains the more systematic offset in this galaxy. Investigating this is beyond the scope of this work, however, for our purposes, these observed variations can serve as rough guide for 'systematic' uncertainties present in our derived |**B**| versus n_H relations.

From our comparison between the CR+ and MHD+ simulations, it is clear that at typical ISM densities in the warm ionized medium (WIM), warm neutral medium (WNM), cold neutral medium (CNM), and molecular phase, cosmic rays do not alter typical magnetic field strengths at a given gas density, though m12m CR+ exhibits systematically lower field strengths, this owing more to galaxy–galaxy variation than to cosmic ray effects. While CRs and magnetic

fields are known to influence each other via plasma instabilities (e.g. Bell 2004), these effects are well below our resolution scale (~ 66 pc at n_H of 1 cm^{-3}, see Hopkins et al. 2018), and have very little effect on galaxy-scale magnetic fields. Thus, while they may influence the 'average' magnetic field strength within a galaxy, it would be indirectly, through changing the overall mass budget at different gas densities or in different phases, moving along the same |**B**| – n_H relation.

We have demonstrated that in some cases, CRs do appear to indirectly lower magnetic fields in the lowest density gas. We have confirmed that this offset is not a result of the overall mass offset between CR+ and MHD+ simulations, by comparing the 'm11' simulations (order of magnitude lower mass haloes) run with MHD+, which do not exhibit such an offset in field strength at a given gas density. Moreover, inspection shows that the offset seen in Fig. 1 (right-hand panel) is not coming from supernova bubbles (the HIM), nor from any particular position within the disc mid-plane (measuring these trends just at the solar circle versus averaged over the whole disc shows the same effect). And we show below that in the outer CGM (far from the galaxy), magnetic field strengths are roughly the same in the MHD+ and CR+ simulations. The systematic difference appears to manifest primarily in the 'inner CGM' or 'disc–halo interface' – tenuous gas between the mid-plane and $\sim$ a few kpc above the disc. In Section 4, we discuss how this is not a direct effect of including CR physics, but rather a second-order effect of the dynamical influence of CRs in this region.

3.2 Pressure budget of the ISM and CGM

In this section, we examine the density dependence of energy densities in the simulations, allowing us to see in which regions of parameter space the magnetic pressure can dominate. Notably, in

---

[3]While this offset at higher gas densities is noteworthy, we are cautious about how much to interpret this, given that it is much smaller than the intrinsic scatter in |**B**| at a given number density.
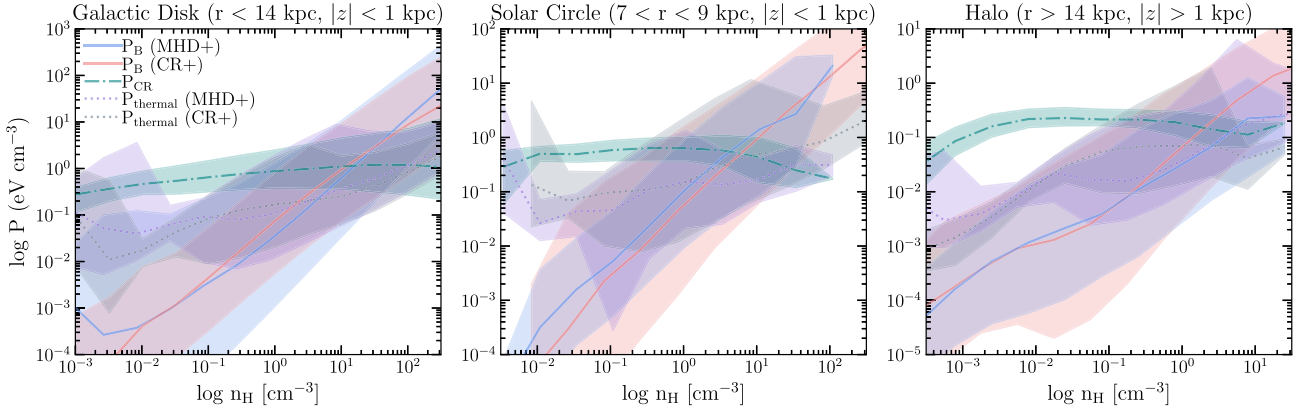
Figure 2. Pressure budget as a function of gas density, for various regions in the simulations of m12i. Here, we show magnetic pressure, P_B, with blue and coral solid lines (for MHD+ and CR+, respectively), thermal pressure, $P_{thermal}$, with purple and grey dotted lines (MHD+ and CR+, respectively) and CR pressure, P_{CR}, with teal dash-dotted line for the CR+ run. The lines represent the means for each density bin and shaded regions show 5–95 percentile intervals (approximate 2σ). Left-hand panel: galactic disc, centre: approximate solar circle, right-hand panel: halo/CGM. In the galactic disc, cosmic rays are in pressure equilibrium with magnetic energies at typical ISM densities ($n_H \sim 1$–10 cm^{-3}), indicating that equipartition assumptions may hold. In the halo, however, magnetic fields are subdominant to cosmic rays in the diffuse phase which fills the CGM volume, and not in equilibrium with thermal pressure.

our CR+ simulations, the cosmic ray energy density (e_{CR}) at 1 GeV is evolved self-consistently, allowing us to examine whether commonly adopted assumptions about equipartition between magnetic and CR energy densities hold in these simulations.

In Fig. 2, we present the magnetic, thermal, and CR pressures (defined as $P_B \equiv |B|^2/8\pi$, $P_{thermal} \equiv n_H k_B T$, $P_{CR} \equiv (\gamma_{CR} - 1) e_{CR}$), respectively) as a function of n_H for different regions of m12i. Note that P_B is also equivalent to u_B, the magnetic energy density. At densities of around 1–10 cm^{-3}, the magnetic energy density is in approximate equipartition with that of CRs, especially in the 'Solar circle' (Fig. 2, middle). This is in agreement with observational constraints in the Solar neighbourhood (Strong, Moskalenko & Reimer 2000; Beck 2001). Equipartition between these various pressures does not hold generally; in our simulations, we see that the CR pressure dominates in the low density ($n_H < 1$ cm^{-3}) gas. This can be understood by the fact that CRs are able to diffuse across field lines, and are thus more weakly functions of the gas density compared to magnetic and thermal pressures. Furthermore, the exact n_H at which the magnetic and CR pressures are equal varies with distance from the galactic centre, comparing the 'Solar circle' and halo regions to the whole disc. Notably, when considering all cells in the galactic disc of m12i (CR+), we find that a mean $\log_{10}(\frac{P_B}{P_{CR}})$ of ~ -1, with a standard deviation ~ 1.

In the halo, however, magnetic fields do not reach equipartition strengths except at higher densities than the majority of gas in the CGM. Thus, in CR-pressure dominated haloes like those of the FIRE galaxies (see also Ji et al. 2020) one would overestimate the magnetic field strength when using the common assumption of equipartition applied to observations. In our simulations, the CR energy density is much larger than the magnetic energy density in the halo. For a constant diffusivity (as these simulations assume), the CR energy density decreases as $\sim r^{-1}$ far from the galaxy, while for an isothermal halo with flux freezing, $|B| \sim r^{-4/3}$, falls more rapidly (Ji et al. 2020). But we caution that this is of course sensitive to the assumptions of how CRs propagate – the diffusivity may not be constant in nature, and many models that fit the MW Solar system constraints equally well can produce a more-rapidly declining P_{CR} with radius (see Hopkins et al. 2021c).

Furthermore, in the halo, it appears that magnetic fields are in near-equipartition with the thermal pressure at densities of 1–10 cm^{-3}, but for diffuse halo gas which fills most of the volume, the magnetic fields are subdominant to thermal pressure. This is consistent with previous studies which found plasma $\beta >> 1$ in halo gas (Su et al. 2018; Butsky et al. 2020; Ji et al. 2020), but is in contrast to results found by Pakmor et al. (2020), which may have more to do with the differing feedback models and numerical implementations, as we discuss further in Section 4. The relation between thermal and magnetic energy densities in our simulations is in contrast to models which predict fields at equipartition pressure with thermal pressure terms, thought to aid in accretion of cool CGM gas (Pakmor et al. 2016; Butsky & Quinn 2018; Prochaska et al. 2019). At high gas densities ($>\sim 50$ cm^{-3}), magnetic pressures dominate over thermal pressures, but perhaps not over the turbulent/dispersion pressure, which was explored in the ISM of FIRE-2 simulations by Gurvich et al. (2020).

Equipartition between cosmic rays and magnetic fields is an assumption whose validity may be scale-dependent due to the propagation of cosmic rays in the ISM from their injection sites at SNe (Beck 2015; Seta & Beck 2019). In Fig. 3, we examine the scale-dependence of equipartition between cosmic rays and magnetic fields in the ISM and disc–halo interface (the very inner CGM) of m12i (CR+) by visualizing the ratio of mass-weighted projections of the magnetic and cosmic ray pressures ($\frac{\int P_B d\ell}{\int P_{CR} d\ell}$). These projections are computed using the routine for line-of-sight integrated quantities described in Section 2, where for the face-on projection we utilize the same convention described therein, and for the edge-on visualization we integrate the line of sight along $\pm$ 14 kpc from the galactic centre.

We find that in the ISM, equipartition is valid on large (> 1 kpc) scales, consistent with observational constraints (Stepanov et al. 2014) and recent theoretical work using idealized simulations of magnetized discs (Rappaz et al. 2022). However, this equipartition is not universal, and regions where equipartition holds are primarily cospatial with the density distribution in spiral structures, with large-scale cavities where the ratio of pressures is as low as 10^{-3}. On small scales, pressure ratios as high as 10^3 are apparent, coincident with dense molecular complexes along the line of sight.
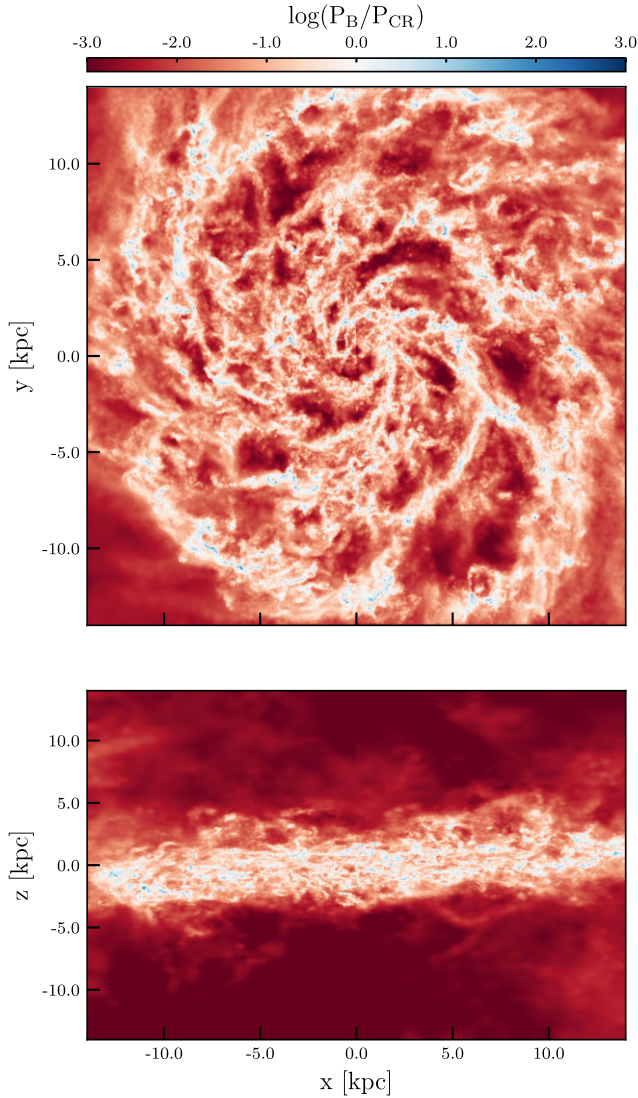
Figure 3. Logarithm of the ratio between magnetic and cosmic ray pressures in m12i (CR+) ($\frac{\int P_B d\ell}{\int P_{CR} d\ell}$), for a face-on projection in the top panel and edge-on projection in the bottom panel. We see that equipartition (white regions) holds on large (> 1 kpc) scales in the galactic disc, cospatially with spiral structure, however with large deviations in inter-arm regions (dark red pockets). On small scales, equipartition does not hold in regions of high magnetic energy density within dense, molecular gas (small, blue regions).

3.3 Magnetic fields in the cold, neutral/molecular ISM: comparison to Zeeman splitting

In this section, we compare the magnetic field amplitude in our simulations to observations of cold neutral and molecular gas in the Milky Way.

3.3.1 Line-of-sight magnetic field strength versus H I column density

The most comprehensive compilation of observations of magnetic field strengths in the cold phases of the ISM has been presented by Crutcher et al. (2010). These estimates rely on observations of the Zeeman effect, which can be used to probe the line-of-sight component of the magnetic field towards diffuse H I clouds and giant molecular clouds (GMCs).
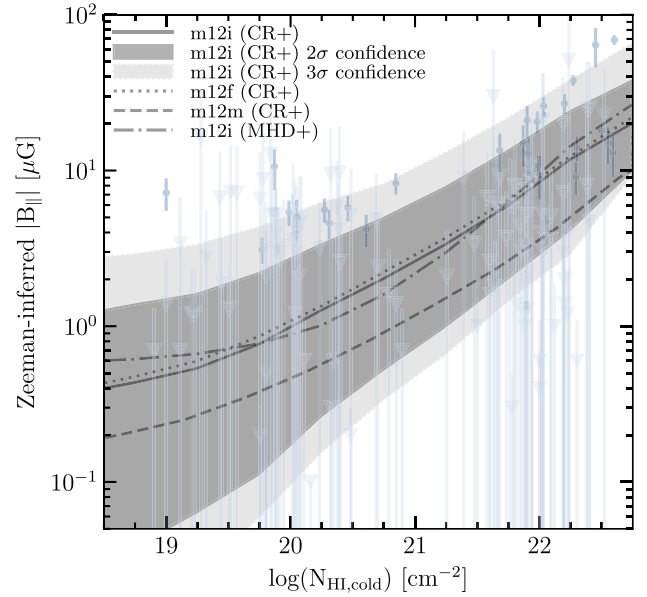

Figure 4. $B_{\parallel,\mathrm{Zeeman-inferred}}$ (equation 1) versus cold neutral-hydrogen column density for face-on projections of m12i, m12f, and m12m (CR+). The black solid line shows the median value at each column density bin for sightlines passing through the galactic disc for m12i, with the same for m12f (CR+) and m12m (CR+) shown with dotted and dashed lines. The results are unchanged if restricted to the solar circle. Shaded regions show 5–95 percentile and 1–99 percentile (approximately 2σ and 3σ confidence regions) for m12i (CR+). Light blue points show observational measurements from Crutcher (2012) and associated 1σ error bars. Non-detections are shown as inverted triangles with $+3\sigma$ upper error bars. Our CR+ simulations show good agreement with the observational data, however; they are slightly more discrepant at the low column density end due to sightlines probing more diffuse atomic gas, which exhibit lower field strengths compared to the MHD+ simulations.

To directly compare with these observations, we integrate the line-of-sight (parallel) component of the magnetic field in the simulations, $B_{\parallel}$, weighted by the cold, neutral hydrogen mass, to obtain a 'Zeeman-inferred' magnetic field. Specifically, we construct sightlines through a face-on projection of the disc, and use the routine described in Section 2 of Hopkins et al. (2005) to calculate the Zeeman-inferred magnetic field as:

$$B_{\parallel,\mathrm{Zeeman-inferred}} = \frac{\int_L n_{\mathrm{HI,cold}} B_{\parallel} \, d\ell}{\int_L n_{\mathrm{HI,cold}} \, d\ell}, \tag{1}$$

where the integration is performed along, ℓ, the path-length through the disc. The cold fraction observed in Zeeman absorption is estimated as $n_{\mathrm{HI,cold}} \sim n_H e^{-T/50\,\mathrm{K}}$ following Crutcher et al., but our results are insensitive to this threshold temperature for any values between $T = 50 - 500$ K as for these cutoff temperatures, the sightlines are still effectively weighted by the dense gas along the line of sight.

Fig. 4 shows the relation between $B_{\parallel,\mathrm{Zeeman-inferred}}$ and column density (N_{HI}) for the CR+ simulations as well as the observational data. Here, the N_{HI} of interest is the same cold, neutral-hydrogen column density, $\int n_{\mathrm{HI,cold}} \, d\ell$. The variables required to compute these line-of-sight values are self-consistently calculated in the simulation and require no further modelling. We have compared a set of sightlines computed using the same method uniformly sampling the entire galactic disc, versus those only sampling the solar circle (7–9 kpc), and find that the results at a given N_{HI} are nearly identical.

We find that there is reasonable agreement between the Zeeman-inferred magnetic field and the observations across the range of column densities; i.e. the majority of the Zeeman observations lie within the scatter of the mock Zeeman measurements for both the CR+ (Fig. 4) and MHD+ (not shown) simulations. However, there is qualitatively poorer agreement at low N_{HI}, especially in m12m (CR+), where the mock Zeeman measurements lie below the majority of the observations. We attribute this to an overall decrease in the total magnetic field strength relative to the MHD+ simulations, which was shown in Fig. 1, due to sightlines probing more diffuse atomic gas (see Ji et al. 2020, who show that the CR+ simulations do feature significantly more cold atomic gas at low densities $n_H \sim$ 0.1–1 cm^{-3}, due to CR pressure support leading to lower thermal pressures at a given gas temperature).

It is also important to note that observations do not probe these diffuse sightlines very robustly, and the constraints in the low N_{HI} regime are mostly upper limits.

There are some caveats to these mock observations: these are not full radiative transfer calculations of the Zeeman splitting of spectral lines in individual clouds, nor is any of our simulations a perfect analogue to the Milky Way. However, the comparisons shown here demonstrate that the simulated galaxies reproduce the observed Milky Way magnetic field strength–column density relation at the order-of-magnitude level.

3.3.2 Zeeman-inferred field strengths and gas densities

In this section, we examine the relation between the Zeeman-inferred $|B_{\parallel}|$ and the 3D gas density which is often discussed in the star formation literature (for a review see Crutcher 2012). Particularly of interest are the results of Crutcher et al. (2010) examined in the previous section, now in a different observational plane which depends on methodology for determining 3D cloud densities. In Fig. 5, we study the relation between Zeeman-inferred magnetic field strength and 3D gas density at the Solar circle in our simulated galaxies.

It is not usually possible to determine the mean density $n_{HI,\,cold}$ of the individual Zeeman absorbers from observations, and since it is well-known that the absorbers are small structures along the line-of-sight, using a quantity like $\int_L n_{HI,\,cold}\,d\ell / \int_L d\ell$ would severely underestimate their typical densities. So instead, we compare two approaches. First, a root-mean-squared (rms) or cold-gas mass weighted density, similar to what one might (ideally) estimate via cold gas line emission, which appropriately weights for clumping along the line of sight:

$$n_{HI,M_{CNM}} = \frac{\int_L n_{HI,cold}^2 d\ell}{\int_L n_{HI,cold} d\ell}. \quad (2)$$

Secondly, we approximate the method from Crutcher et al. (2010) and Crutcher (2012), which assumes that the H I spin temperature T_{spin} gives the kinetic temperature $T = T_{spin}$ of the gas, which itself is in thermal pressure equilibrium with a universal constant pressure, so that everywhere $n_{HI,\,cold} \cdot T = 3000\,\mathrm{K\,cm^{-3}}$. This gives

$$n_{HI,T_{CNM}} = 3000\,\mathrm{K\,cm^{-3}}\,\frac{\int_L n_{HI,\,cold}\,d\ell}{\int_L n_{HI,\,cold}\,T\,d\ell}. \quad (3)$$

Fig. 5 shows the $B_{\parallel,Zeeman-inferred}$ versus density for the two different density estimators. We see that $B_{\parallel,Zeeman-inferred}$ versus $n_{HI,M_{CNM}}$ gives at least a broadly similar trend to the 'true' theoretical $|\mathbf{B}|$ versus n_H in Fig. 1, with a differing normalization by a factor of $\sim$2 owing to the geometric effect of measuring solely the line-of-sight component
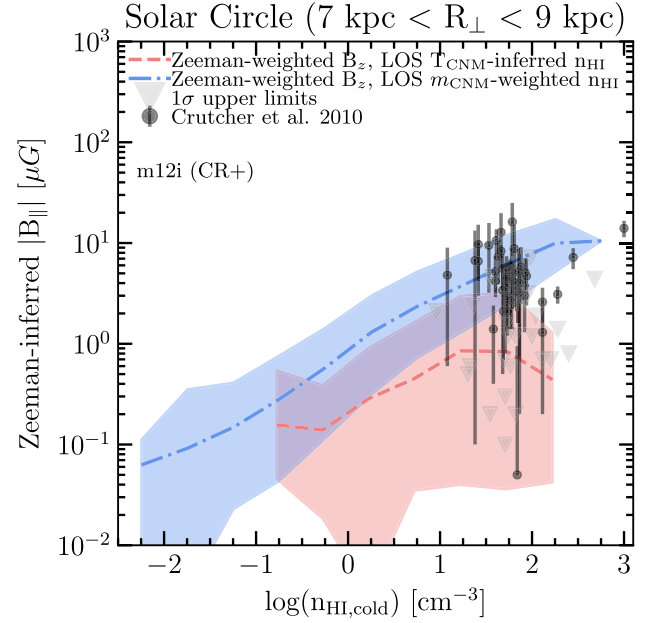

Figure 5. Zeeman-inferred $|B_{\parallel}|$ versus cold, neutral hydrogen number density for m12i (CR+). Each line shows the mean Zeeman-inferred $|B_{\parallel}|$ at each number density bin. The coral line shows $|B_{\parallel}|$ versus $n_{HI,\,T_{CNM}}$ (equation 3), which is the number density inferred from the LOS cold, neutral hydrogen weighted-temperature assuming thermal pressure equilibrium. The blue line also shows the Zeeman-inferred $|B_{\parallel}|$, but plotted against $n_{HI,M_{CNM}}$ (equation 2), which is the LOS cold mass-weighted density. The black points show observations from (Crutcher et al. 2010) and associated 1σ errorbars, and non-detections are shown with inverted grey triangles. The shaded regions show the 5–95 percentiles (approximately 2σ). The results are nearly identical for the MHD+ run, and for m12f and m12m (not shown). The relation between $|B_{\parallel}|$ and $n_{HI,M_{CNM}}$ is broadly consistent with the purely theoretical values of $|\mathbf{B}|$ versus n. However, when using $n_{HI,\,T_{CNM}}$, the relation is flattened due to thermal pressure equilibrium being a poor approximation in the cold ISM, thus not faithfully tracing the 'true' density.

of the magnetic field. While $B_{\parallel,Zeeman-inferred}$ is consistent with the observed data, the relation between $B_{\parallel,Zeeman-inferred}$ and $n_{HI,\,T_{CNM}}$ is flattened significantly, and we find that this effect remains even if we isolate the sightlines with dense complexes ($n_H > 300\,\mathrm{cm^{-3}}$) along the path-length, or draw sightlines through those dense complexes themselves, rather than sampling sightlines through the entire disc at the Solar circle. This is because there is very little correlation, over the dynamic range here, between $n_{HI,\,T_{CNM}}$ and either $n_{HI,M_{CNM}}$ or the true gas density n_H from which the Zeeman absorption originates. The poor correlation owes to the fact that: (1) thermal pressure equilibrium is not a particularly good approximation in the cold ISM, where other forms of pressure (including magnetic as we show in Fig. 2, turbulent, and cosmic ray) all dominate over thermal, and the conditions are highly dynamic (Grudić et al. 2021), and (2) even if thermal pressure equilibrium were reasonable, there is not a single thermal pressure across all clouds in all locations in the Milky Way (e.g. towards the galactic centre, it is well-known that cloud pressures are much higher). As a result, using $n_{HI,\,T_{CNM}}$, which not only assumes constant thermal pressure, but a single value of thermal pressure across all sightlines, introduces considerable scatter in the x-axis of Fig. 5, essentially 'smearing out' the correlation. Recall that our values of $|B_{\parallel}|$ are the same for all sightlines, so the effect on the normalization depends on which densities are most heavily sampled. If we sampled denser true sightlines more numerously, as

in the Crutcher et al. (2010) analysis, then the normalization of this curve would be the same as their favoured value.

3.4 Magnetic fields in the ionized ISM and CGM: Comparison to rotation and dispersion measures

3.4.1 Comparison to pulsar RMs and DMs in the galaxy

In this section, we compare the simulations with observational probes of the magnetic field in the ionized medium, primarily through use of Faraday rotation and dispersion measure. Faraday rotation occurs due to the interaction of light with a magneto-ionic plasma, causing the plane of polarization to rotate as a function of the electron density and magnetic field strength. The average magnetic field along the line of sight ($|\langle B_\parallel \rangle|$) can be determined through the rotation measure if an independent constraint is found on the electron density, n_e, given by the dispersion of radio pulses. The dispersion measure is dependent on the thermal electron column density and we compute the DMs along the mock line-of-sight as $DM = \int n_e d\ell$. The RMs are computed with the standard definition (Beck 2015):

$$RM = \frac{e^3}{2\pi m_e^2 c^3} \int_L n_e \mathbf{B} \cdot \mathbf{dl} = 0.808 \int_L n_e(cm^{-3}) \mathbf{B}(\mu G) \cdot \mathbf{dl}(pc),$$
(4)

where e is the electron charge, m_e is the electron mass, c is the speed of light, and the integration is performed along the path-length ℓ.

To compare the synthetic measurements as expected from our MW-analogues to MW pulsar observations, we use the same line-of-sight computation routine described in Section 2 of dividing the galactic disc into 'slabs' to determine RMs and DMs. For Zeeman splitting, it makes no difference if we integrate arbitrarily large sightlines 'outside' of the disc because these have a very small probability of intercepting cold atomic H I. However, for RM/DM measurements, it is important that we sample sightlines of appropriate depths through the disc (similar to those for the actual observed Galactic pulsars), and not simply integrate all sightlines to $\pm\infty$, because then the predicted DM would be completely dominated by the cumulative contribution from halo and IGM ionized gas.

In Fig. 6 we show the synthetic RM versus the synthetic DM for m12i, along with MW pulsar data from the Australian Telescope National Facility (ATNF) catalogue (Manchester et al. 2005) and from the Low-Frequency Array (LOFAR) (Sobey et al. 2019a). Our simulated RMs and DMs are in good agreement with the observations, with most of the observational measurements towards MW pulsars falling within 1σ of the simulation scatter and almost all within 2σ. This indicates that we find similar magnetic field strengths and geometries averaged over sightlines through the disc in the warm, ionized medium to what is seen in the Milky Way. Between the CR+ and MHD+ runs, we find negligible differences in the inferred properties of the magnetic field in the WIM, consistent with our previous results that CRs do not substantially affect the magnetic properties and observables in the ISM.

As many have noted (Simard-Normandin & Kronberg 1980; Rand & Kulkarni 1989; Han et al. 1999; Sobey et al. 2019b, a), a naive estimate of $|\langle B_\parallel \rangle| \sim 1.2\,|RM|/DM$ gives $|\langle B_\parallel \rangle| \sim 0.1 - 10\,\mu G$ with a median around $\sim 1\,\mu G$. Note that $|\langle B_\parallel \rangle|$, which is probed by $1.2\,|RM|/DM$, differs from $\langle B_\parallel \rangle$ in that the absolute value is taken after the line-of-sight averaging. This, in turn, means that $1.2\,|RM|/DM$ will be sensitive to reversals of the magnetic field along the line of sight, underpredicting the true magnitude of $\langle B_\parallel \rangle$ and thereby informing us about the coherence of the magnetic field along the line of sight.
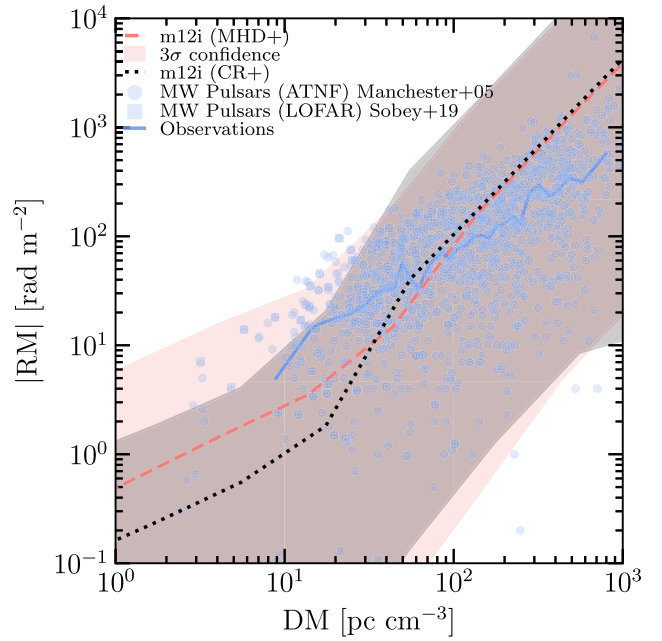

Figure 6. |RM| versus DM for sightlines through the discs of m12i MHD+ and CR+ (coral and black, respectively). Lines indicate the mean $|RM|$ in each DM bin and the shaded region represents 1–99 percentiles (approximate 3σ). The blue points show observations of Milky Way pulsars using LOFAR done by Sobey et al. (2019a) and as queried by Seta & Federrath (2021) from the ATNF Pulsar Catalogue (Manchester et al. 2005), with the solid blue line showing the median |RM| of both sets of observations at each DM, with 30 bins of equal numbers of observations.

In our simulated discs, we see that $1.2\,|RM|/DM$ underestimates the actual average values of $\langle |B| \rangle$ weighted by the thermal electron density by a factor of ~ 2.5. Note that $\langle |B| \rangle$, which is the linear weighted average of the magnitude of B, is a factor of 1.2–2.2 smaller than the 'rms' **B** often quoted in the literature, for example in Seta & Federrath (2021), and is given by $\langle \mathbf{B}^2 \rangle^{1/2}$, where the multiplicative factor depends on the clumping of the magnetic field. Along sightlines drawn through our simulated WIM, this factor appears to be ~ 1.2.

In the next section, we will explore how RMs and DMs trace magnetic fields in the CGM, and how CRs may have an impact on these observables.

3.4.2 RMs and DMs in the ISM and CGM to distant observers

Recently, there has been a surge of theoretical and observational interest in the properties (including magnetic fields) of the CGM, so we extend our comparison to galactocentric radii $\sim 10 - 200$ kpc. Note that we restrict to RMs and DMs here (as opposed to Zeeman splitting), since the CGM gas is predominantly ionized and there do not exist Zeeman splitting data for the CGM.

In Fig. 7 we visualize the RMs, DMs, and $B_\parallel$ seen in a face-on projection of the galaxy zoomed in on the central 40 kpc, while in Fig. 8 we present visualizations out to 200 kpc. Inspection reveals sign flips (field reversals) in RM or $B_\parallel$ on both large and small scales, with notable features including the spiral arms and large-scale inflows joining the disc – these features are consistent with observations, as discussed below.

Constraints on the strength and geometry of ISM magnetic fields in nearby galaxies come from intensity and RM measurements
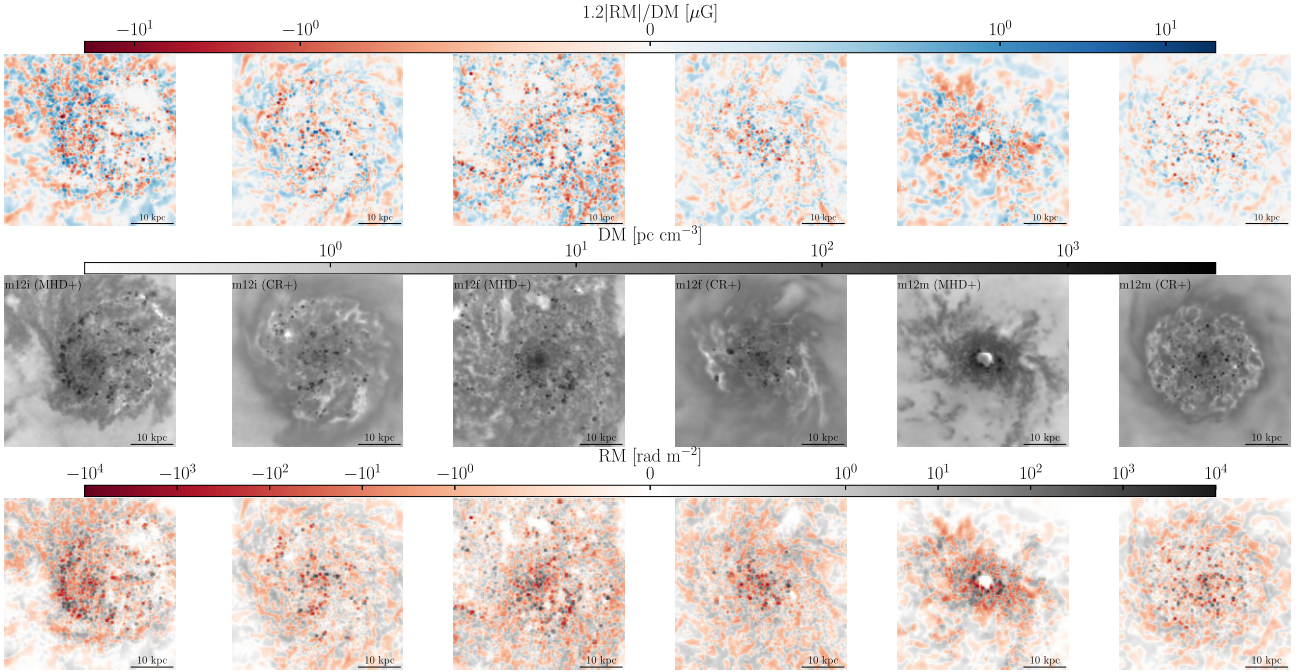
Figure 7. Visualizations of various line-of-sight quantities within the central 40 kpc. **Row 1:** Line-of-sight RM/DM-inferred magnetic field strength. **Row 2:** Dispersion Measures. **Row 3:** Rotation Measures, with m12i (MHD+ and CR+), m12f (MHD+ and CR+), and m12m (MHD+ and CR+) from left to right. Our simulations exhibit small-scale reversals in the sign of RMs similarly to observations, indicative of small-scale field reversals due to explicit treatment of stellar feedback and partially resolved ISM phase structure.

of diffuse radio emission (Beck 2015; Han 2017). Fletcher et al. (2011) published the most detailed map of RMs, towards the face-on spiral galaxy M51 by inferring RM through modelling the variation of the synchrotron polarization angle with wavelength at 3–6 cm. Qualitatively, the RM visualization is similar, with sign flips on all observed scales. This is also similar to what is inferred from modelling the spatial distribution of MW pulsar RMs and DMs, and variations in dust polarization and synchrotron to construct galactic magnetic field maps (e.g. Jansson & Farrar 2012; Haverkorn 2015; Han 2017; Beck et al. 2019). The same appears to be true in the LMC, from visual inspection (Gaensler et al. 2005).

Briefly, Fletcher et al. (2011) explicitly note that they cannot measure the shape of the distribution of RMs in M51 (as their observed RM distribution is noise-dominated), but they can estimate the intrinsic rms value of |RM| averaged over the Galactic disc (giving $\langle |RM|^2 \rangle^{1/2} \sim 10 \, \mathrm{rad \, m^{-2}}$, about half the measured rms before accounting for observational errors), which is similar to rms values we obtain in our simulated discs in Fig. 7 of around $\sim 20 \, \mathrm{rad \, m^{-2}}$.

We quantify the dependence of various quantities of interest as a function of galactocentric radius in the CGM in Fig. 9. We present cylindrically averaged radial profiles of RM, DM, and $\langle |B|^2 \rangle^{1/2}$ in the CGM. A few trends are evident. First, we see that while there is considerable detailed spatial structure in Fig. 8, the cylindrically averaged median profiles (Fig. 9) are quasi-universal radial power laws in impact parameter R, with median $DM \propto R^{-1}$ (expected for gas in an isothermal-sphere type profile with 3D $\rho \propto r^{-2}$), $\langle |B_\parallel| \rangle \propto R^{-1}$ and correspondingly $|RM| \propto R^{-2}$, on average. The range of slopes for each is roughly ± 0.3. The intrinsic scatter about the trend is large, however, ~ 1 dex in $|RM|$, and subsequently similar in $1.2|RM|/DM$. Interestingly, the trend in $\langle |B_\parallel| \rangle$ is a bit shallower than what we might expect for isotropic flux-freezing ($|\mathbf{B}| \propto \rho^{2/3} \propto R^{-4/3}$), closer to what we might expect for $\langle |B_\parallel| \rangle \propto \rho^{1/2}$ in the CGM, similar to the trend seen in the ISM, in Fig. 5.

Secondly, there are some small but systematic offsets between the MHD+ and CR+ simulations. In the inner CGM approaching the disc ($r \sim 10$ kpc), $B_\parallel$ is a factor of 1.5–2 higher in MHD+, directly related to the offset in Fig. 1. Far from the disc, the DMs are a factor of 1.5–2.5 lower in MHD+: this owes to the lack of CR pressure (able to support a larger 'weight' of CGM gas) and inefficient galactic outflows leading to more accretion from the CGM on to the galaxy (Ji et al. 2020, 2021; Hopkins et al. 2021b). In contrast, within the disc, this leads to higher DMs for MHD+. Together, these mean that while typical ISM RMs are larger in the more massive, more dense MHD+ simulations, the RM profile in the CGM is nearly identical.

Thirdly, we see that the inferred $\langle B_\parallel \rangle \sim 1.2|RM|/DM$ underestimates the median $|B_\parallel|$, or $\langle |\mathbf{B}_\parallel| \rangle$ of gas along the LOS by a factor of ~ 5–7. The fields are close to isotropic in this statistical and cylindrically averaged sense, where we are averaging multiple lines of sight along annuli at a given galactocentric radius. So, this means that $\langle |\mathbf{B}| \rangle \sim 2\langle |\mathbf{B}_\parallel| \rangle$, which means on average $|RM|/DM \sim 0.1 \langle |\mathbf{B}| \rangle$ where the averaged terms are weighted by electron density in the same manner as RM. We have confirmed that this owes primarily to cancellation due to random field components along the LOS; crudely, this systematic offset is equivalent to the statement that the coherence length of the magnetic field is ~ 10 per cent the size of the system contributing to RM (i.e. ~ 20 kpc – comparable to the halo scale length – in the outer CGM).

While there is no observational measurement of RM from the CGM around any $\sim L_*$ galaxy, a number of studies measuring RMs from background fast radio bursts (FRBs) and other bright radio sources have placed upper limits which can be compared to the predictions of our simulations. At the radii shown in Fig. 9, we plot the most stringent upper limits to date, specifically the upper limit towards an FRB found in Prochaska et al. (2019) and the 3σ upper limits quoted as a function of impact parameter in the
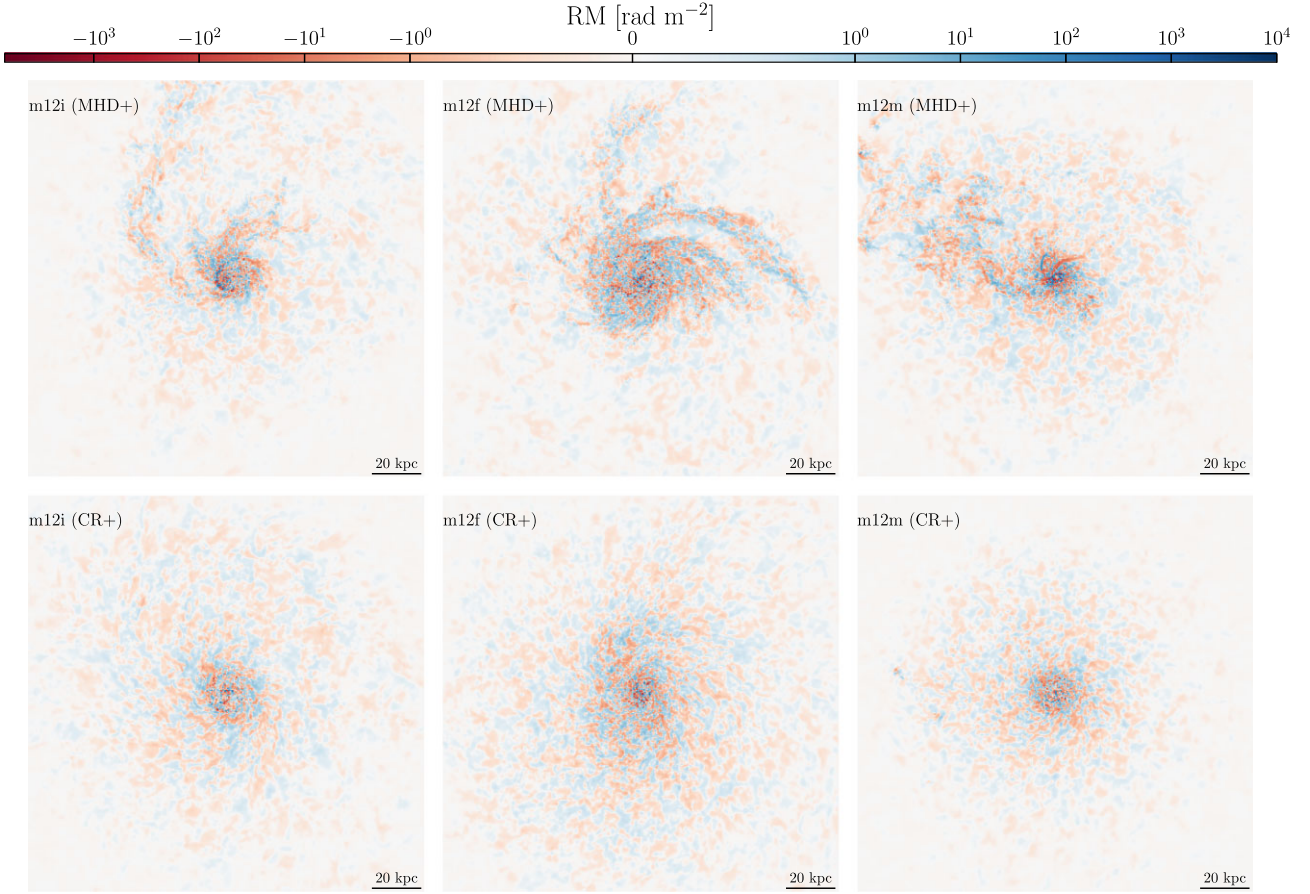
Figure 8. Face-on visualizations of synthetic rotation measures out to a projected radius of 200 kpc as seen by an external observer towards an ideal background source. **Row 1:** MHD+ simulations. **Row 2:** CR+ simulations, with m12i, m12f, m12m from left to right. Large scale gas inflows and spiral structure can be seen, as well as sign reversals in RM on both large and small scales. In m12m MHD+, an in-falling satellite galaxy and tidal tail can be observed.

FRB study of Lan & Prochaska (2020).[4] At even larger impact parameters $\gtrsim 500$ kpc (not shown), Ravi et al. (2016) place a 2σ upper limit on $\langle \mathbf{B}_\parallel \rangle_{IGM}$ of 2.1×10^{-2} µG, and O'Sullivan et al. (2020) measure a 2σ upper limit $|RM| < 1.9$ rad m^{-2} and constrain the IGM magnetic field strength to be $\langle |\mathbf{B}| \rangle_{IGM} < 4 \times 10^{-3}$ µG, both from FRB detections. We see that the simulations are easily consistent with all of these limits, but the data are not yet particularly constraining. Still, with much larger FRB samples expected in the near future from DSA-110, CHIMES, and CHORD it should be possible to improve these upper limits by an order of magnitude or more, potentially reaching detection thresholds at least in the inner CGM (CHIME/FRB Collaboration 2018; Kocz et al. 2019; Vanderlinde et al. 2019; Connor & Ravi 2021). Further observational data are needed to delineate between differing physical and numerical schemes which predict order of magnitude differences in halo field strengths from our results, discussed below (Pakmor et al. 2020).

---

[4]Note that while the FRBs used in Prochaska et al. (2019), Lan & Prochaska (2020) have measured RMs, these RMs are almost certainly strongly dominated by the contribution from the FRB host galaxy, with an unknown additional contribution from the FRB source and IGM, so the authors can place only a statistical upper limit on the contribution to the measured RM from the CGM of the foreground $\sim L_*$ galaxy.

4 DISCUSSION AND CONCLUSIONS

The results in this work have presented probes of the magnetic field as traced in different gas phases; cold, dense and neutral ISM gas (T ~ 100 K, $n_H \gtrsim 10$ cm^{-3}), warm ionized ISM gas ($n_H \sim 0.1$ cm^{-3}, T $\gtrsim 6000$ K), and hot, diffuse CGM gas (T $\gtrsim 10^6$ K, $n_H \sim 0.001$ cm^{-3}). Due to having resolved phase structure of the ISM in these simulations, we are able to meaningfully compare these tracers to their observational counterparts without use of additional modeling or assumptions, and are thus able to both (a) test whether observational assumptions apply in these simulations and (b) comment on how two physical models (MHD+, CR+) compare in their predictions of the observables.

We investigated how the magnetic field properties vary in two types of simulations of the same galaxies: MHD+ and CR+. We find general agreement in the scaling of the overall relation of $|\mathbf{B}|$ versus number density in all of the simulations, but with a modest offset between the MHD+ and CR+ runs of a factor of $\sim 2 - 10$ primarily at very diffuse ISM densities (n < 0.01 cm^{-3}) which increases towards more diffuse densities and is more systematic for m12m, with an offset of a factor of ~ 2 at (n > 1 cm^{-3}). This difference at very diffuse ISM densities, as mentioned above, arises primarily due to differences in the 'inner CGM.'

The 'inner CGM' is precisely where previous studies (Booth et al. 2013; Simpson et al. 2016; Girichidis et al. 2018; Buck et al. 2020; Ji et al. 2020, 2021; Chan et al. 2021; Hopkins et al.
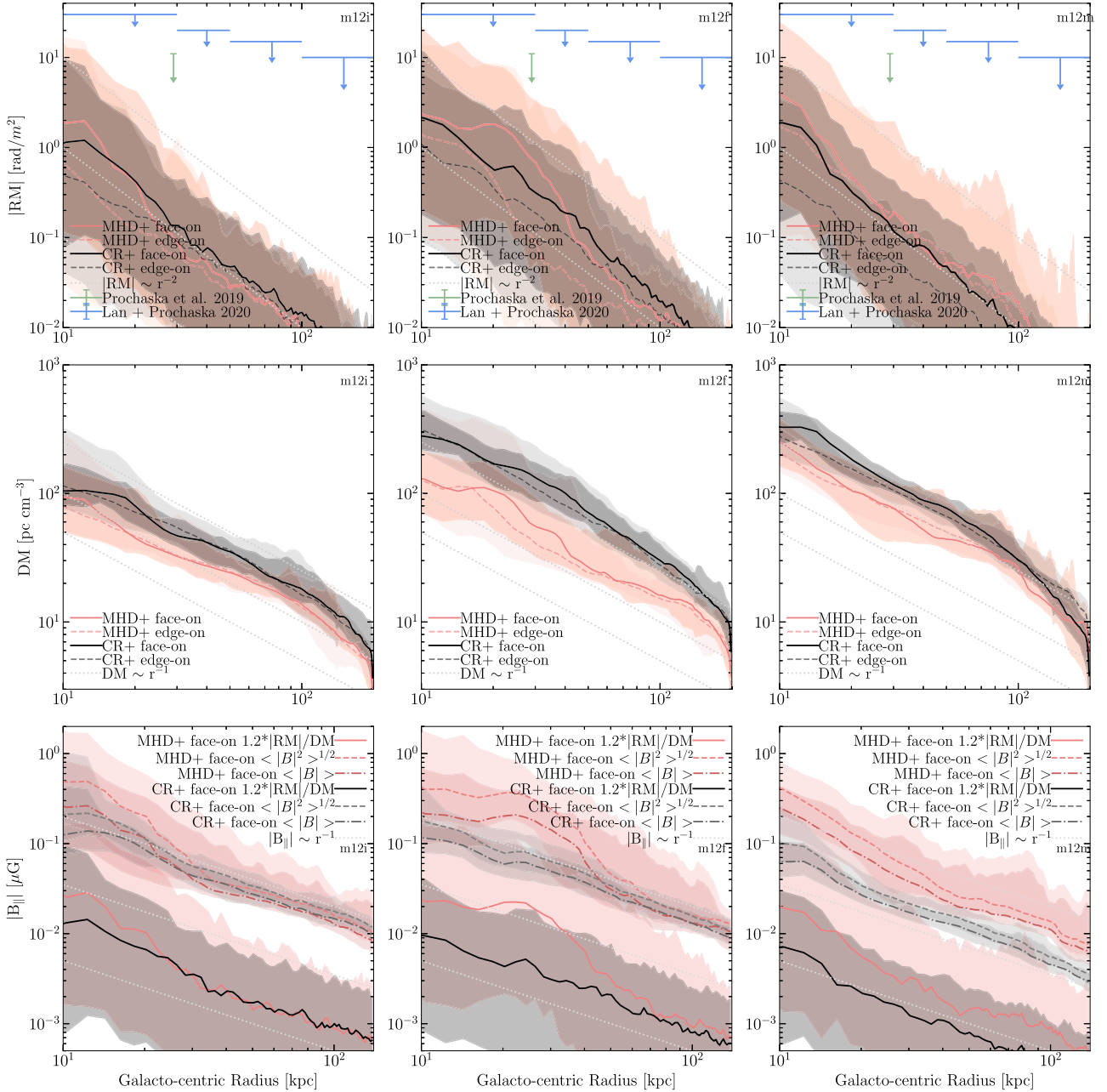
Figure 9. Rotation measure (|RM|), dispersion measure (DM), and $|B_\parallel|$ profiles as a function of galactocentric radius (R). **Row 1:** RM profiles with MHD+ simulations (m12i, m12f, m12m from left to right) shown in coral and CR+ simulations shown in black. Face-on and edge-on profiles are denoted by solid and dashed lines, respectively. Each line shows the median at a given radial bin. The shaded regions show 5–95 percentile intervals (approximate 2σ error-bars). The green point shows an upper-limit from the RM measured towards an FRB in the halo of a galaxy with $M_* \sim 10^{10.69}$ M$_\odot$ studied by Prochaska et al. (2019). The blue lines show 3σ upper limits on RMs in the CGM from a sample of high-redshift radio sources studied by Lan & Prochaska (2020). The grey dotted lines show representative power laws as a visual guide. **Row 2:** Dispersion measure (DM) profiles with the same colour and line style conventions as the RM profiles. **Row 3:** Estimates of $|B_\parallel|$ as determined from 1.232 RM/DM shown in solid lines, and 'true' $< |B| >$ and $< |B|^2 >^{1/2}$ shown with dot-dashed and dashed lines, respectively. Our RM and DM profiles are not in tension with the existing observations, which are not yet constraining. The predicted 1.2 |RM|/DM profiles are consistent with what would be expected for those of an isothermal sphere. Subtle systematic offsets between MHD+ and CR+ RM profiles exist directly due to the offset in diffuse gas near the disc at low R, and far from the disc in the DM profiles due to CR pressure support. Our $|B_\parallel|$ profiles indicate that RM/DM significantly underpredicts $< |B| >$ averaged over large lines of sight as well as the rms $< |B|^2 >^{1/2}$ by a factor of ~ 15–20.

2021b) have shown CRs can play a dramatic role influencing the dynamics of galactic fountains and outflows. Specifically, in simulations without cosmic rays, MW-mass galaxies at low redshifts have their outflows 'trapped' by CGM pressure, creating high-velocity fountains with rapid recycling (Muratov et al. 2015; Anglés-

Alcázar et al. 2017; Gurvich et al. 2020; Stern et al. 2021; Hafen et al. 2022), while in the CR+ simulations, the added CR pressure gradient both maintains gas acceleration and reduces the pressure barrier to outflows, allowing disc outflows to smoothly escape to the outer halo (references above). We directly confirm that, as a

result, the velocity dispersion of the low-density inner-CGM gas which drives the offset of |**B**| versus n_{gas} is lower in the CR+ simulations by a factor of $\sim$2–3. This, in turn, means that magnetic fields experience significantly less amplification by 'turbulent' or fountain flows in this range of conditions due to recycling of outflows (Martin-Alvarez et al. 2018), and greater adiabatic attenuation, since the escaping outflow will reduce the magnetic field strength of any advected fields from the disc via flux-freezing as the outflowing gas expands. This can explain some of the offset in |**B**| versus number density between MHD+ and CR+ galaxies, but not the whole difference.

From our CR+ simulations, which self-consistently evolve the GeV CRs which dominate the CR energy budget, we are able to make predictions for the relative strengths of magnetic, thermal, and CR pressures in different gas phases. We find that in the disc, equipartition assumptions between CRs and magnetic fields (as is often assumed for estimating magnetic field strengths from observations of diffuse radio emission; Chyzy et al. 2011; Beck 2015) may hold on large scales, and at typical ISM densities ($L > 1$ kpc, $n_H \sim 1$–10 cm^{-3}); however in the CGM, this assumption breaks down. Similarly, assumptions of equipartition between thermal and magnetic pressures in the CGM appear to be invalid given the predictions of our model; however, details of this depend on how CRs are treated and their interplay with metal-enriched, actively cooling gas (Prochaska et al. 2019; Hopkins et al. 2021a). That being said, in both the halo and the ISM, we generally see a plasma $\beta \ll 1$ in cold/neutral dense gas (reaching values as low as 5×10^{-5}), and $\beta \gg 1$ in low density, mostly ionized gas (reaching values as high as 7×10^8), consistent with most previous theoretical studies (Su et al. 2018; Butsky et al. 2020; Ji et al. 2020).

We compare ISM magnetic field values inferred from Zeeman measurements within the Galaxy for the cold, neutral medium, and find broad agreement (Fig. 4). In detail, there are some differences between runs, primarily that the offset in magnetic field strength at lower gas densities results in CR+ simulations predicting slightly lower values of $B_{\parallel}$ relative to the MHD+ simulations at lower column densities, which probe more of the diffuse gas. This results in slightly poorer agreement at lower column densities ($\log_{10}(N_H) < 21$ cm^{-2}) between the existing observations of Crutcher (2012) and our simulations. While the CR+ simulations exhibit slightly lower values of $B_{\parallel}$ relative to the MHD+ simulations, we note that the overall qualitative agreement with the observations is not notably different between the two physical models.

The physical relations of $B_{\parallel}$ versus density (Fig. 5) for both the MHD+ and CR+ simulations agree considerably well with the Solar circle diffuse H I observations of Crutcher et al. (2010). The observations of interest span higher densities ($n > 300$ cm^{-3}), where there is little difference in the magnetic field strength of the MHD+ and CR+ simulations.

As discussed in Section 3.3.2, the poor correlation between $n_{HI,T_{CNM}}$ and $n_{HI,M_{CNM}}$ flattens the relation between |$B_{\parallel}$| and n. This may explain some aspects of the Crutcher et al. (2010) analysis, which compiles Zeeman observations from three types of clouds (diffuse H I, IR dark, and dense molecular) of varying densities using three different tracers (H I, OH, CN). It is important to note that *within any* one sample: i.e. within any one 'type of cloud' or within any one tracer, there is no statistically significant trend of |$B_{\parallel}$| with $n_{HI,T_{CNM}}$ in the Crutcher et al. (2010) data. This leads, for example, to their conclusion that the Zeeman-inferred |$B_{\parallel}$| is approximately constant in diffuse gas with $n < 300$ cm^{-3}, which are exclusively sampled by diffuse H I – it is only when the different data sets, each of which samples different median density ranges (e.g. diffuse H I at

10^1–$10^{2.5}$ cm^{-3}, dark clouds for $10^{3.5}$–$10^{4.5}$ cm^{-3}, dense molecular clumps at $10^{5.5}$–$10^{6.5}$ cm^{-3}) are combined that the underlying trend (quite similar to what we predict here) can be observed. Here, we show that detecting the predicted trend within the dynamic range of densities probed by H I Zeeman data alone (a factor of $\sim$10–30 in gas density) requires a 3D gas density estimator which is accurate to much better than this dynamic range (i.e. to within a factor of $\sim$2 or so).

In visually examining the synthetic rotation measures for our simulated galaxies, we find variations of the sign of RM on small scales as well as large scales, with quantitative values in agreement upper limits placed in the haloes of L_* galaxies by Prochaska et al. (2019), Lan & Prochaska (2020). Zooming in on the disc, we find RM sign reversals on small scales in a manner qualitatively similar to the RM maps of M51 produced by Fletcher et al. (2011), with little to no correlation of the RMs with galactic structure, differing from work done by Pakmor et al. (2018), who performed a similar study of the RM by analysing a MW-analogue from the Auriga simulations. Our synthetic RMs show a less ordered, more turbulent magnetic field in better agreement with the observations, which is primarily indicative of the effect of explicit stellar feedback and resolution of the ISM phase structure, in contrast to the subgrid 'effective equation-of-state' model used for the ISM in that work.

For the warm, ionized phase of the ISM of our simulated galaxies, we find good agreement with RMs and DMs towards Milky Way pulsars. While the mean RM/DM-inferred magnetic field strength ubiquitously underpredicts the mean 'true' rms |**B**| in the disc, at the column densities of interest, it traces $B_{\parallel}$ averaged along sightlines through the disc.

While we primarily focus the discussion of the RMs, DMs, and subsequent inferred estimates of $B_{\parallel}$ on the halo in Fig. 9, we find good qualitative agreement between the intrinsic dispersion of the RM as inferred from synchrotron polarization at 3 and 6 cm by Fletcher et al. (2011), with the caveat that the methodology of our synthetic RMs does not aim to faithfully reproduce that of Fletcher et al. (2011) and contains information averaged over large (~ 280 kpc deep) sightlines rather than solely arising from the disc. In the region that is primarily of interest for these synthetic background point source RMs, i.e. the halo, the MHD+ and CR+ profiles converge, independently of resolution.

Our CGM-focused results suggest that use of RMs and DMs towards point sources as measures of $B_{\parallel}$ underestimate the 'true' magnetic field strength in the halo at a given galactocentric radius by about a dex. This is consistent with work done by Seta & Federrath (2021), who found that in the presence of driven subsonic, transonic, and supersonic turbulence, the standard deviation of the average parallel component of the magnetic field is about an order of magnitude less than the true rms magnetic field strength of the box. Here, in Fig. 9, the RM/DM estimate traces effectively the ionized-mass-weighted parallel component of the magnetic field, and $< |B|^2 >^{1/2}$ averaged over the extensive (240 kpc) lines of sight probes the root mean square magnetic field strength. This result may be of particular importance for observers looking to characterize the magnetic field strengths in the haloes of galaxies towards background FRBs, implying that RM/DM estimates may be a factor of ~ 10 lower than the true halo magnetic field strength. From our estimate of how well the RM/DM-inferred $B_{\parallel}$ traces the 'true' rms $\langle |B|^2 \rangle^{1/2}$ we infer that the coherence length is ~ 50 per cent the characteristic length scale in the ISM (on order of the disc scale height), and $\sim$10–20 per cent of the characteristic length scale in the CGM, on order the halo scale length. This result on the coherence length is similar to predictions or the large-scale coherence length towards MW

pulsars from random walk models described by Seta & Federrath (2021).

Notably, the predictions of RMs and $\langle|B|^2\rangle^{1/2}$ of the Auriga cosmological zoom-in simulations presented in Pakmor et al. (2020) are a factor of ~ 10 higher than those computed from the FIRE simulations. The Auriga simulations use an effective equation-of-state model of the ISM Springel & Hernquist (2003) in contrast to the explicit treatment of feedback used in our simulations. The typical intercell spacing in the CGM of the haloes of FIRE and Auriga are similar ($\sim$ kpc), and both are notably turbulent (see Ji et al. 2020), however it remains unclear what dominates magnetic amplification in the halo, and whether resolving the inertial scale of turbulence in the CGM will be key to generating accurate halo magnetic fields. We note also that varying the σ_p, σ_h, and α_ψ divergence cleaning and slope-limiter terms (see Hopkins & Raives 2016) by factors of $\sim$5 does not affect the magnetic field properties of these simulated galaxies, indicating that the magnetic field strength is set by physical processes rather than numerics. We have shown that in our simulations with resolved ISM phase structure, the magnetic field strengths very reasonably agree with existing constraints from the Milky Way and M51, however the halo remains uncertain. Present observational constraints are unable to distinguish between these different physical models and numerical treatments, and future observations (e.g. Kocz et al. 2019) will be key for understanding CGM magnetic fields.

5 SUMMARY AND FUTURE WORK

In this paper, we have analysed the magnetic fields in the multiphase ISM and CGM in a set of high-resolution, cosmological simulations from the FIRE-2 project, run with two different physical models (MHD+, CR+). We analyse the differences between the magnetic fields in simulations run with each model, and compare forward-modelled observables tracing magnetic fields in the ISM and CGM to existing observational constraints.

In summary, our conclusions are as follows:

(i) Inclusion of CRs in simulations of galaxy formation does not directly affect the magnetic field strengths in the ISM at a given gas density, though there are modest differences in the lowest density gas ($n < 0.01$ cm^{-3}) due to dynamical effects of CRs in the disc–halo interface (the inner most region of the CGM). The main effect of CRs is indirect, causing the average $|B|$ in those galaxies' less massive, less dense discs to be lower than their MHD counterparts, moving along the same scaling relations between $|B|$ and n_H.

(ii) Our predicted relation for $|B|$ versus 3D gas density n_H is consistent with that of flux freezing in spherically symmetric and non-spherical geometry ($|B| \sim n_H^{2/3}$ or $|B| \sim n_H^{1/2}$).

(iii) Equipartition between magnetic, thermal, and cosmic ray pressures is achieved in our simulated galactic discs at typical ISM densities ($n \sim 1$–10 cm^{-3}). Equipartition between magnetic and cosmic ray energy densities primarily holds on large (> 1 kpc) scales, cospatial with the spiral structure of our galactic disks, and fails in the interarm regions and on small scales in the presence of dense molecular gas.

(iv) In the haloes of our simulated galaxies, equipartition between magnetic pressures and cosmic ray pressures does not hold, and neither does equipartition between thermal and magnetic pressures ($\beta >> 1$).

(v) Our simulated magnetic field strengths in the cold, neutral ISM agree well with existing Zeeman observations in the Milky Way, and indicate observational estimates of the 3D gas density in diffuse H I from spin temperatures may be noisy due to thermal pressure

equilibrium being a poor assumption in this phase of the ISM. This can act to obfuscate existing correlations between $|B_{||}|$ and n_H for $n_H < 300$ cm^{-3}.

(vi) The magnetic field strengths in the warm, ionized ISM of our simulated galaxies are in agreement with observations of Milky Way pulsars and M51 as inferred through rotation measures and dispersion measures.

(vii) Our synthetic rotation measures as a function of impact parameter are in agreement with existing constraints from FRBs probing the haloes of L_* galaxies, however there is a large parameter space occupied in this plane by various physical and numerical models. Future surveys which will localize 100s of FRBs per year will be crucial to constraining current model predictions.

(viii) In the CGM, our CR+ simulations exhibit slightly enhanced DMs relative to the MHD+ simulations in the inner CGM ($R \sim 50$–100 kpc) due to cosmic ray pressure support.

(ix) Our simulations' comparison of 1.2 $|RM|$/DM ($\langle B_{||}\rangle$) to the 'rms' field $\langle|B^2|^{1/2}\rangle$ indicates that observational estimates of magnetic fields in the haloes of L_* galaxies from FRBs may underpredict the true rms field strength by a factor of 15–20, in qualitative agreement with previous works.

Our study provides motivation to more closely study the magnetic fields in these simulations (e.g. turbulent magnetic field amplification and its connection to feedback models), and to generate detailed mock observations using radiative transfer codes like POLARIS (Reissl, Wolf & Brauer 2016). This will enable detailed comparison with more indirect magnetic field tracers, such as synchrotron intensities, magnetic field morphologies inferred from polarized dust and synchrotron emission (Borlaff et al. 2021), and resolved Zeeman spectra.

We will also explore predictions for different galaxy types (e.g. dwarfs or starbursts), and redshift evolution, which may help shed light on magnetic field amplification mechanisms. It is also important to continue to explore different physics: as we noted above, our CR+ models adopt a highly simplified empirical (constant-diffusivity) assumption for CR transport, and previous work (Hopkins et al. 2021c) has shown that other observationally allowed models with variable diffusivity can produce different result (so even if CRs are present, reality may closely resemble our MHD+ simulations, for example).

Additionally, our simulations neglect the effects of AGNs, which may be an important component of the feedback budget for L_* galaxies (e.g. Wellons et al. 2022; Feldmann et al. 2022, and references therein). Further understanding of galactic magnetic fields and their tracers from a theoretical perspective may lead to insight on questions related to survival and infall of cool CGM gas, star formation efficiency in dense gas, and the ability of cosmic rays to influence galactic properties via transport along magnetic field lines.

under NASA contract NAS5-26555. Numerical calculations were run on the Caltech compute cluster 'Wheeler,' allocations AST21010 and AST20016 supported by the NSF and TACC, and NASA HEC SMD-16-7592. The Flatiron Institute is supported by the Simons Foundation.

DATA AVAILABILITY

The data supporting the plots within this article are available on reasonable request to the corresponding author. A public version of the GIZMO code is available at http://www.tapir.caltech.edu/~phopkins/Site/GIZMO.html. FIRE-2 simulations are publicly available (Wetzel et al. 2022) at http://flathub.flatironinstitute.org/fire, though simulations including the physics of MHD and cosmic rays like those analysed in this study are not yet publicly available. Additional data, including initial conditions and derived data products, are available at https://fire.northwestern.edu/data/.

REFERENCES

Anglés-Alcázar D., Faucher-Giguère C.-A., Kereš D., Hopkins P. F., Quataert E., Murray N., 2017, MNRAS, 470, 4698

Beck R., 2000 , in Philosophical Transactions of the Royal Society A. Astronomy, Physics and Chemistry of H^+_3. Royal Society

Beck R., 2001, Space Sci. Rev., 99, 243

Beck R., 2015, A&AR, 24, 4

Beck R., Krause M., 2005, Astron. Nachr., 326, 414

Beck R., Shukurov A., Sokoloff D., Wielebinski R., 2003, A&A, 411, 99

Beck R., Chamandy L., Elson E., Blackman E. G., 2019, Galaxies, 8, 4

Bell A. R., 2004, MNRAS, 353, 550

Bellardini M. A., Wetzel A., Loebman S. R., Faucher-Giguère C.-A., Ma X., Feldmann R., 2021, MNRAS, 505, 4586

Booth C. M., Agertz O., Kravtsov A. V., Gnedin N. Y., 2013, ApJ, 777, L16

Borlaff A. S. et al., 2021, ApJ, 921, 128

Boulares A., Cox D. P., 1990, ApJ, 365, 544

Bryan G. L., Norman M. L., 1998, ApJ, 495, 80

Buck T., Pfrommer C., Pakmor R., Grand R. J. J., Springel V., 2020, MNRAS, 497, 1712

Burbidge G. R., 1956, ApJ, 124, 416

Butsky I. S., Quinn T. R., 2018, ApJ, 868, 108

Butsky I., Zrake J., Kim J.-h., Yang H.-I., Abel T., 2017, ApJ, 843, 113

Butsky I. S., Fielding D. B., Hayward C. C., Hummels C. B., Quinn T. R., Werk J. K., 2020, ApJ, 903, 77

Chan T. K., Kereš D., Hopkins P. F., Quataert E., Su K. Y., Hayward C. C., Faucher-Giguère C. A., 2019, MNRAS, 488, 3716

Chan T. K., Kereš D., Gurvich A. B., Hopkins P., Trapp C., Ji S., Faucher-Giguère C.-A., 2022, MNRAS

CHIME/FRB Collaboration, 2018, ApJ, 863, 48

Chyzy K. T., Wezgowiec M., Beck R., Bomans D. J., 2011, A&A, 529, 94

Connor L., Ravi V., 2021, preprint (arXiv:2107.13692)

Crutcher R. M., 2012, ARA&A, 50, 29

Crutcher R. M., Wandelt B., Heiles C., Falgarone E., Troland T. H., 2010, ApJ, 725, 466

Desiati P., Zweibel E. G., 2014, ApJ, 791, 51

Feldmann R. et al., 2022, preprint (arXiv:2205.15325)

Fermi E., 1949, Phys. Rev., 75, 1169

Fletcher A., Beck R., Shukurov A., Berkhuijsen E. M., Horellou C., 2011, MNRAS, 412, 2396

Gaensler B. M., Haverkorn M., Staveley-Smith L., Dickey J. M., McClure-Griffiths N. M., Dickel J. R., Wolleben M., 2005, Science, 307, 1610

Girichidis P., Naab T., Hanasz M., Walch S., 2018, MNRAS, 479, 3042

Grudić M. Y., Guszejnov D., Hopkins P. F., Offner S. S. R., Faucher-Giguère C.-A., 2021, MNRAS, 506, 2199

Gurvich A. B. et al., 2020, MNRAS, 498, 3664

Guszejnov D., Grudíc M. Y., Offner S. S., Boylan-Kolchin M., Faucher-Gigère C. A., Wetzel A., Benincasa S. M., Loebman S., 2020, MNRAS, 492, 488

Hafen Z. et al., 2022, MNRAS, 514, 5056

Han J. L., 2017, ARA&A, 55, 111

Han J. L., Manchester R. N., Qiao G. J., 1999, MNRAS, 306, 371

Haverkorn M., 2015, in Lazarian A., de Gouveia Dal Pino E. M., Melioli C., eds, Astrophysics and Space Science Library, Vol. 407, Magnetic Fields in Diffuse Media. Springer, Berlin, p. 483

Hopkins P. F., 2015, MNRAS, 450, 53

Hopkins P. F., Raives M. J., 2016, MNRAS, 455, 51

Hopkins P. F., Hernquist L., Martini P., Cox T. J., Robertson B., Di Matteo T., Springel V., 2005, ApJ, 625, L71

Hopkins P. F. et al., 2018, MNRAS, 480, 800

Hopkins P. F. et al., 2020, MNRAS, 492, 3465

Hopkins P. F., Butsky I. S., Panopoulou G. V., Ji S., Quataert E., Faucher-Giguere C.-A., Keres D., 2022, preprint (arXiv:2109.09762)

Hopkins P. F., Chan T. K., Ji S., Hummels C. B., Kereš D., Quataert E., Faucher-Giguère C.-A., 2021b, MNRAS, 501, 3640

Hopkins P. F., Squire J., Chan T. K., Quataert E., Ji S., Kereš D., Faucher-Giguère C.-A., 2021c, MNRAS, 501, 4184

Jansson R., Farrar G. R., 2012, ApJ, 757, 14

Ji S., Oh S. P., McCourt M., 2018, MNRAS, 476, 852

Ji S. et al., 2020, MNRAS, 496, 4221

Ji S., Kereš D., Chan T. K., Stern J., Hummels C. B., Hopkins P. F., Quataert E., Faucher-Giguère C.-A., 2021, MNRAS, 505, 259

Kocz J. et al., 2019, MNRAS, 489, 919

Krumholz M. R., Federrath C., 2019, Front. Astron. Space Sci., 6, 7

Kulsrud R., Pearce W. P., 1969, ApJ, 156, 445

Lan T. W., Prochaska J. X., 2020, MNRAS, 496, 3142

Manchester R. N., Hobbs G. B., Teoh A., Hobbs M., 2005, AJ, 129, 1993

Marinacci F., Pakmor R., Springel V., 2014, MNRAS, 437, 1750

Martin-Alvarez S., Devriendt J., Slyz A., Teyssier R., 2018, MNRAS, 479, 3343

Muratov A. L., Kereš D., Faucher-Giguère C.-A., Hopkins P. F., Quataert E., Murray N., 2015, MNRAS, 454, 2691

Ntormousi E., Tassis K., Del Sordo F., Fragkoudi F., Pakmor R., 2020, A&A, 641, A165

O'Sullivan S. P. et al., 2020, MNRAS, 495, 2607

Pakmor R., Springel V., 2013, MNRAS, 432, 176

Pakmor R., Marinacci F., Springel V., 2014, ApJ, 783, L20

Pakmor R., Pfrommer C., Simpson C. M., Springel V., 2016, ApJ, 824, L30

Pakmor R., Guillet T., Pfrommer C., Gómez F. A., Grand R. J., Marinacci F., Simpson C. M., Springel V., 2018, MNRAS, 481, 4410

Pakmor R. et al., 2020, MNRAS, 498, 3125

Pfrommer C., Werhahn M., Pakmor R., Girichidis P., Simpson C. M., 2022, MNRAS, 515, 4229

Prochaska J. X. et al., 2019, Science, 366, 231

Rand R. J., Kulkarni S. R., 1989, ApJ, 343, 760

Rappaz Y., Schober J., Girichidis P., 2022, MNRAS, 512, 1450

Ravi V. et al., 2016, Science, 354, 1249

Reissl S., Wolf S., Brauer R., 2016, A&A, 593, A87

Rieder M., Teyssier R., 2017, MNRAS, 472, 4368

Rodrigues L. F., Chamandy L., Shukurov A., Baugh C. M., Taylor A. R., 2019, MNRAS, 483, 2424

Seta A., Beck R., 2019, Galaxies, 7, 45

Seta A., Federrath C., 2021, MNRAS, 502, 2220

Shukurov A., Snodin A. P., Seta A., Bushby P. J., Wood T. S., 2017, ApJ, 839, L16

Simard-Normandin M., Kronberg P. P., 1980, ApJ, 242, 74

Simpson C. M., Pakmor R., Marinacci F., Pfrommer C., Springel V., Glover S. C. O., Clark P. C., Smith R. J., 2016, ApJ, 827, L29

Sobey C. et al., 2019a, MNRAS, 484, 3646

Sobey C. et al., 2019b, MNRAS, 484, 3646

Springel V., Hernquist L., 2003, MNRAS, 339, 289

Steinwandel U. P., Beck M. C., Arth A., Dolag K., Moster B. P., Nielaba P., 2019, MNRAS, 483, 1008

Steinwandel U. P., Dolag K., Lesch H., Moster B. P., Burkert A., Prieto A., 2020, MNRAS, 494, 4393

Steinwandel U. P., Dolag K., Lesch H., Burkert A., 2022, ApJ, 924, 26

Stepanov R., Shukurov A., Fletcher A., Beck R., La Porta L., Tabatabaei F., 2014, MNRAS, 437, 2201

Stern J. et al., 2021, ApJ, 911, 88

Strong A. W., Moskalenko I. V., Reimer O., 2000, ApJ, 537, 763

Su K. Y., Hopkins P. F., Hayward C. C., Faucher-Giguère C. A., Kereš D., Ma X., Robles V. H., 2017, MNRAS, 471, 144

Su K.-Y., Hayward C. C., Hopkins P. F., Quataert E., Faucher-Giguère C.-A., Kereš D., 2018, MNRAS, 473, L111

Tritsis A., Panopoulou G. V., Mouschovias T. C., Tassis K., Pavlidou V., 2015, MNRAS, 451, 4384

van de Voort F., Bieri R., Pakmor R., Gómez F. A., Grand R. J. J., Marinacci F., 2021, MNRAS, 501, 4888

Vanderlinde K. et al., 2019, in Canadian Long Range Plan for Astronomy and Astrophysics White Papers. p. 28, preprint (arXiv:1911.01777)

Wang P., Abel T., 2009, ApJ, 696, 96

Wellons S. et al., 2022, preprint (arXiv:2203.06201)

Werhahn M., Pfrommer C., Girichidis P., 2022, MNRAS, 508, 4072

Wetzel A. et al., 2022, preprint (arXiv:2202.06969)

This paper has been typeset from a TEX/LATEX file prepared by the author.